International Journal of Plasticity 111 (2018) 234–252

Contents lists available at ScienceDirect

International Journal of Plasticity

journal homepage: www.elsevier.com/locate/ijplas

Understanding thermal alleviation in cold dwell fatigue in titanium alloys

Zebang Zheng[a,*], Adam Stapleton[b], Kate Fox[b], Fionn P.E. Dunne[a]

[a] Department of Materials, Imperial College London, London, SW7 2AZ, United Kingdom
[b] Rolls-Royce plc, Derby, DE24 9BJ, United Kingdom

ARTICLE INFO

Keywords:
Cold dwell fatigue
Crystal plasticity
Titanium alloys
Microstructure
Temperature sensitivity
Aero-engine discs
Thermal alleviation

ABSTRACT

Dwell fatigue facet nucleation has been investigated in isothermal rig disc spin tests and under anisothermal in-service engine conditions in titanium alloy IMI834 using α-HCP homogenised and faithful α-β lamellar microstructure crystal plasticity representations. The empirically observed facet nucleation and disc failure at low stress in the isothermal spin tests has been explained and originates from the material rate sensitivity giving rise to soft grain creep accumulation and hard grain basal stresses which increase with fatigue cycling until facet nucleation. The α-HCP homogenised model is not able to capture this observed behaviour at sensible applied stresses. In contrast to the isothermal spin tests, anisothermal in-service disc loading conditions generate soft grain slip accumulation predominantly in the first loading cycle after which no further load shedding nor soft grain creep accumulation is observed, such that the behaviour is stable, with no further increase in hard grain basal stress so that facet nucleation does not occur, as observed empirically. The *thermal alleviation*, which derives from in-service loading conditions and gives the insensitivity to dwell fatigue dependent on the temperature excursions, has been explained. A stress-temperature map for IMI834 alloy has been established to demarcate the ranges for which the propensity for dwell fatigue facet nucleation is high, threatening or low.

1. Introduction

Cold dwell fatigue was first recognised through an air accident in the 1970s due to the failure of two titanium fan disks in Rolls-Royce RB211 engines (Bache, 2003; Song and Hoeppner, 1989). A significant lifetime reduction, known as dwell debit, occurs when titanium alloys are subjected to cyclic loading with stress hold at maximum magnitude (dwell period) in each cycle at low temperatures (e.g. $T < 0.4T_m$) (Cuddihy et al., 2017; Evans and Bache, 1994; Evans and Gostelow, 1979; Hasija et al., 2003; Qiu et al., 2014). Dwell sensitivity of titanium alloys has been an important research interest since then.

Facet crack nucleation on basal slip planes of hexagonal closed packed (HCP) crystals is argued to be responsible for the early service failure of near α titanium alloys (Sinha et al., 2006). The local crystallographic orientation combination with respect to the loading direction was found to cause load shedding during the dwell period in which stresses are redistributed from 'soft' grains into the adjacent 'hard' grains (Hasija et al., 2003). This local creep behaviour results in high grain boundary stresses (Zheng et al., 2016a) and may induce the subsequent crack nucleation. Much work has been carried out to understand the mechanistic basis of the load shedding phenomena. Hasija et al. (2003) first reported the stress redistribution from soft to hard-orientated grains in single α phase Ti-6Al using crystal plasticity (CP) modelling. Huang et al. (2012) demonstrated the load partitioning between the soft (matrix) and

* Corresponding author.
E-mail address: zebang.zheng12@imperial.ac.uk (Z. Zheng).

https://doi.org/10.1016/j.ijplas.2018.07.018
Received 10 April 2018; Received in revised form 29 June 2018; Accepted 25 July 2018
Available online 26 July 2018

hard (precipitates) grains due to the creep behaviour using in-situ neutron diffraction technique. Sinha et al. (2006) studied near α Ti-6242 alloy and have shown the prismatic slip accumulated in the soft grain results in dislocation pileups and hence inducing elevated stress fields more likely to initiate cracks on basal planes in the adjacent hard grain. Extensive modelling work by Dunne et al. (Dunne and Rugg, 2008a, 2008b; Dunne et al., 2007c) and Ghosh et al. (Ghosh and Anahid, 2013; Ghosh and Chakraborty, 2013; Venkataramani et al., 2008) has shown the local stress development under dwell fatigue loading at room temperature using homogenised α phase CP models. Joseph et al. (2018) and Zheng et al. (2017a, 2018) investigated the effect of slip transfer through interfaces on fatigue behaviour of titanium alloys. Bache et al. (1997) found that the dwell debit is reduced by applying lower peak hold stress. Ozturk et al. (2017) using CP modelling also demonstrated that the number of cycles to nucleate facets increases with decreasing the dwell stress.

In all the aforementioned work, the dwell fatigue tests were carried out at near room temperature (e.g. 20 °C); however, temperature also significantly affects load shedding through its influence on the strain rate sensitivity of titanium alloys, and hence their dwell sensitivity. For example, the number of cycles to failure for alloy Ti-6246 under dwell fatigue loading was found to be ~10000 at 20 °C, ~7300 at 80 °C and ~13000 at 150 °C (Bache, 2003). Es-Souni (2001) compared the tensile creep properties between 500 °C and 600 °C of three titanium alloys with different composition. The high temperature creep was found to be controlled by the climb of edge dislocations. Hardt et al. (1999) investigated high-temperature fatigue damage mechanisms in IMI834 alloys up to 650 °C and revealed both the maximum tensile stress and the strain rate of each cycle affect the fatigue life significantly at the considered temperatures. Pototzky et al. (1998) studied the isothermal and thermo-mechanical fatigue (TMF) behaviour of IMI834 alloy between 350 °C and 650 °C. Their results suggest that the stress-strain response under TMF can be predicted by isothermal loading. Furthermore, the fatigue life when the tests were carried out in air is greatly reduced compared to vacuum environment due to the rapid diffusion of oxygen. All the experimental evidence suggests that temperature is an important factor in understanding fatigue, and hence dwell fatigue in aero-engines, but the in-service temperature of titanium fan blades in engines is generally below 350 °C. The modelling work by Zhang et al. (2015) found that load shedding in α Ti-6Al alloy increases with temperature from 20 °C and peaks at about 120 °C followed by a diminution to zero at about 220 °C. This results from the influence of temperature on both the slip system strengths (CRSSs) and strain rate sensitivities. Ozturk et al. (2016) using homogenised α-HCP 3D crystal plasticity finite element modelling with the grain size distribution and orientation distribution fully recognised to investigate the fatigue crack nucleation under isothermal conditions between 300 °C and 600 °C. The simulation results are also able to reproduce the diminution of dwell sensitivity at elevated temperatures as observed experimentally. The atomistic simulations carried out by Ready et al. (2017) demonstrated that Mo atoms in titanium alloys are not able to trap the vacancies for long enough at room temperatures in order to give rise to the observed strain rate sensitivity. This is important in demonstrating that it is not the chemistry (or more particularly the molybdenum) which gives rise intrinsically to the differing dwell behaviours of alloys Ti-6242 and Ti-6246. Zheng et al. (2017b) using discrete dislocation plasticity (DDP) investigated the temperature sensitivity of dwell fatigue in Ti-6242 and Ti-6246 alloys assuming homogenised α-HCP polycrystal representations in both cases. Similar behaviour of temperature-dependent load shedding as for Ti-6Al alloy was found for Ti-6242, and alloy Ti-6246 was found to show dwell sensitivity at higher temperatures of 300 °C. When the α-β basketweave microstructure is fully accounted for in the latter material, it is anticipated that the alloy would not be expected to show any dwell sensitivity. The authors proposed a mechanistic basis for load shedding with respect to temperature at the dislocation scale with respect to purely α (or homogenised α representations of α-β) polycrystals:

(1) At low temperatures, obstacles behave as strong barriers to dislocation motion; creep is less likely to occur during the dwell period, and hence load shedding is not expected.
(2) At high temperatures, obstacles provide weak resistance to dislocation gliding, and dislocation structures reach equilibrium rapidly, even before the stress hold begins, and hence no (further) stress is redistributed during the dwell period.
(3) At intermediate temperatures, dislocations in soft grains gradually build up at soft-hard grain boundaries during the dwell period, and hence strong load shedding can be observed.

The majority of dwell fatigue research has so far focused on isothermal loading conditions, but this is simply unrepresentative of in-service loading which is strongly thermo-mechanical. Indeed, the thermal and mechanical loading interactions have been argued to give rise to resistance to dwell fatigue through a process called thermal alleviation. Thermal alleviation in dwell fatigue implies the reduction of dwell sensitivity in titanium alloys when the thermos-mechanical loading cycle contains elevated (e.g. $\geq$ 200°C) temperatures. In addition, the in-service mechanical loading relevant to aero-engine components gives rise to stresses in dwell-sensitive regions which are way below the macroscopic yield stress for all temperatures of relevance. It remains the case that almost all experimental, lab-based (and modelling) investigations of dwell fatigue address much higher applied stresses (typically 0.90 $\sigma_{0.2}$ or 0.95 $\sigma_{0.2}$) than is relevant to dwell fatigue in components.

The purpose of this study is therefore to address a number of key but outstanding problems in dwell fatigue as follows. (i) An assessment is carried out of crystal plasticity modelling of dwell which utilises homogenised α grains (i.e. grains which are represented with averaged α-β properties but with HCP slip only) versus non-homogenised faithful representation of typical α-β lamellar structures in alloy IMI834 in order to show why dwell fatigue occurs at much lower applied stresses than those close to yield. (ii) Isothermal dwell fatigue (representative of spin tests used by manufacturers) is examined and compared to thermo-mechanical loading representative of in-service conditions and in both cases, crystal plasticity modelling predictions compared directly with industry observed dwell response for the two loading types. (iii) For the in-service (engine) thermo-mechanical response, we address the role of thermal alleviation and provide the underpinning explanation for how it inhibits dwell fatigue. The integration of CP modelling of dwell fatigue with component and in-service industry testing addressed in this paper is unique and identifies the key

purpose for research in this subject; that is, to understand the drivers for dwell facet nucleation for in-service components (as opposed to laboratory samples). As a consequence, the material of interest is the titanium alloy IMI834.

In what follows, a brief presentation of the CP modelling and property determination for IMI834 over the range of temperatures of interest is given. The paper then presents an assessment of the ability of homogenised α-HCP CP models to capture experimental (disc) test dwell fatigue observations, and this is followed by the analysis of the full representation of typical α-β lamellar structures in IMI834 and the corresponding assessment of predicted dwell fatigue response for both the experimental (disc) tests and also for representative thermos-mechanical in-service engine response. A discussion of thermal alleviation and how it diminishes dwell sensitivity is provided together with a comparative analysis of the isothermal versus thermally alleviated dwell responses.

2. Rate and temperature dependent crystal plasticity

Rate and temperature dependent crystal plasticity modelling is utilised in this study (Dunne et al., 2007a) and the slip rule developed in previous work has been demonstrated to capture appropriately the strain rate sensitivity, stress redistribution (load shedding) and cold dwell behaviour in titanium alloys at room temperature (Cuddihy et al., 2017; Zhang et al., 2016; Zheng et al., 2016b) and at higher temperatures (Zhang et al., 2015). The total deformation gradient $\boldsymbol{F}$ is decomposed into elastic, plastic and thermal parts given by

$$\boldsymbol{F} = \boldsymbol{F}^e\boldsymbol{F}^p\boldsymbol{F}^\theta \tag{1}$$

Unless specified otherwise, matrix multiplication is indicated by bold symbols; scalar multiplication in non-bold. The thermal deformation gradient $\boldsymbol{F}^\theta$ represents the lattice deformation from temperature change. The evolution of the gradient is given by (Lee et al., 1997; Ozturk et al., 2016) as

$$\dot{\boldsymbol{F}}^\theta = \dot{T}\boldsymbol{\alpha}\boldsymbol{F}^\theta \tag{2}$$

where T is the temperature, and $\boldsymbol{\alpha}$ is a diagonal tensor with respect to crystallographic coordinates, which gives the thermal expansion anisotropy of the titanium alloy. The plastic velocity gradient $\boldsymbol{L}^p$ includes contributions from all slip systems and is given by

$$\boldsymbol{L}^p = \dot{\boldsymbol{F}}^p(\boldsymbol{F}^p)^{-1} = \sum_i \dot{\gamma}^i \boldsymbol{s}^i \otimes \boldsymbol{n}^i \tag{3}$$

where $\boldsymbol{s}^i$ and $\boldsymbol{n}^i$ are the unit vector along slip direction and slip plane normal of slip system i respectively. Both forward and backward thermally activated dislocation escape from lattice obstacles, e.g. solute atoms, are facilitated giving rise to the rate sensitive slip response (Dunne et al., 2007a). The resultant slip rate of a given slip system i takes the form:

$$\begin{aligned} \dot{\gamma}^i &= 0 && \text{if } |\tau^i| \le \tau_c^i \\ \dot{\gamma}^i &= \rho_m (b^i)^2 \nu_D exp\left(-\frac{\Delta F}{kT}\right)\sinh\left(\frac{(|\tau^i| - \tau_c^i)\Delta V}{kT}\right) && \text{if } |\tau^i| > \tau_c^i \end{aligned} \tag{4}$$

where ρ_m is the mobile dislocation density, b^i the Burgers vector, ν_D the Debye frequency, k the Boltzmann constant, τ^i and τ_c^i are the resolved shear stress and the corresponding critical resolved shear stress (CRSS) on slip system i. The temperature considered in the present study varies from 20 °C up to 370 °C. The intrinsic slip strain rate sensitivity is determined by an activation energy ΔF and a corresponding activation volume $\Delta V = \gamma_0 b^2/\sqrt{\rho_0}$, where γ_0 is a representative shear strain magnitude and ρ_0 is the initial obstacle density.

In order to resolve the time dependent boundary conditions, a time incremental formulation used in the present study may be described as follows: a trial stress state is first determined assuming only elastic deformation occurs in the current time increment. The slip rate is thus determined using Eq. (4) under the trial stress state. If slip occurs, the stress state in the model does not balance with the remote boundary conditions. Hence a new trial stress is calculated using the slip determined previously. Then, in the same way, a new slip rate is calculated under the new trial stress state. The stress balance between material and the boundary conditions is checked and the iterative procedure described above continued until their difference is below a threshold stress value (e.g. 10^{-8}MPa).

The IMI834 alloy, which is used to manufacture aero-engine discs, has been investigated in the present study. It consists of a complex bimodal microstructure with equiaxed α grains, α –β colony structure and some local basketweave structures which are formed under thermo-mechanical heat treatment conditions. The effect of microstructure is addressed later.

2.1. Material property calibration for IMI834 alloy

The experimentally measured temperature dependence of macroscopic (isotropic) elastic modulus of IMI834 is shown in Fig. 1. In this study, the temperature dependence of the elastically anisotropic elastic properties of homogenised α phase is chosen such that the polycrystal response gives the same overall temperature dependence as the experimental measurement. The elastic properties and their temperature dependencies are given by

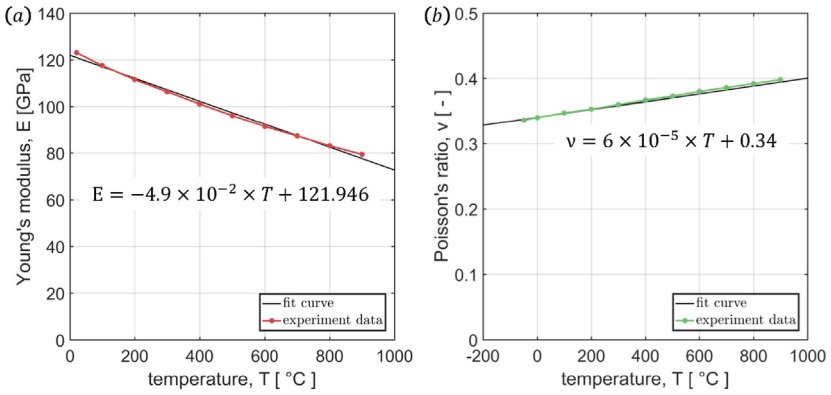

Fig. 1. Experimentally measured macroscopic (a) Young's modulus and (b) Poisson's ratio of IMI834 alloy with temperature (by courtesy of Rolls-Royce plc).

$$
\begin{aligned}
E_1 &= -5.980 \times 10^{-2} \times T + 128.770 \\
E_3 &= -5.980 \times 10^{-2} \times T + 162.770 \\
G_{13} &= -3.845 \times 10^{-2} \times T + 40.000 \\
\nu_{12} &= 9.000 \times 10^{-5} \times T + 0.459 \\
\nu_{13} &= 6.000 \times 10^{-5} \times T + 0.218
\end{aligned} \tag{5}
$$

where modulus takes units of GPa and temperature T units of Celsius (°C). The elastic anisotropy is defined through a local Cartesian coordinate system in which the 1-direction is parallel to the $[\bar{1}2\bar{1}0]$ direction, the 2-direction parallel to $[\bar{1}010]$ and the 3-direction parallel to [0001]. The anisotropic thermal expansion for titanium alloys at low temperatures (< 400 °C) is taken to be $9.5 \times 10^{-6}\ °C^{-1}$ along the 1-direction and $5.6 \times 10^{-6}\ °C^{-1}$ along 3-direction as determined experimentally (Pawar and Deshpande, 1968).

In order to determine slip system properties which capture the appropriate strain rate and temperature sensitivity of IMI834 alloy, a homogenised α phase polycrystal model was established with 3D Voronoi tessellated grains using the VGRAIN software system (Zhu et al., 2014). The average grain size was chosen to be 1000μm simply to be representative of the macrozone size observed in IMI834 alloy, with minimum and maximum sizes taken to be 800μm and 1200μm respectively with a Voronoi regularity parameter of 0.95. In total 216 grains were generated within a 6000μm cube and the overall texture is chosen to be random as shown in Fig. 2.

Displacement-controlled uniaxial tension tests on IMI834 under isothermal conditions provided by Rolls-Royce were utilised to determine 0.2% proof stresses at a strain rate of $5 \times 10^{-5} s^{-1}$ over temperature range 20 °C–400 °C to give

$$\sigma_{0.2} = 0.0022 \times T^2 - 1.6629 \times T + 933.32 \tag{6}$$

The experimental stress-strain data for temperatures of 80 °C, 150 °C and 300 °C were selected to calibrate the intrinsic slip system rate and temperature dependent properties including the activation energy ΔF, activation volume ΔV and the CRSS of a-prismatic slip using the polycrystal model shown in Fig. 2. The ratio of <a>-basal, <a>-pyramidal to <a>-prismatic slip strengths were taken to be identical to those for α phase titanium alloy given in (Zhang et al., 2015, 2016) as 1.125, and 1.00 respectively (see below for details of <$c + a$> strengths). The stress strain responses under the same strain rate as for experiments are shown in Fig. 3(a) and the 0.2% proof stresses at corresponding temperatures are indicated by the symbols. The resulting extracted temperature dependence of the a-prismatic slip system CRSS is given by

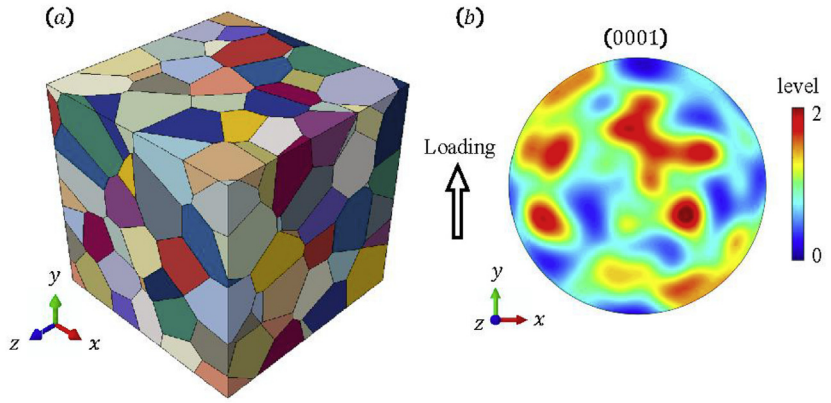

Fig. 2. (a) Homogenised α phase 3D polycrystal model consists of 216 grains with random texture as shown by the pole figure in (b).

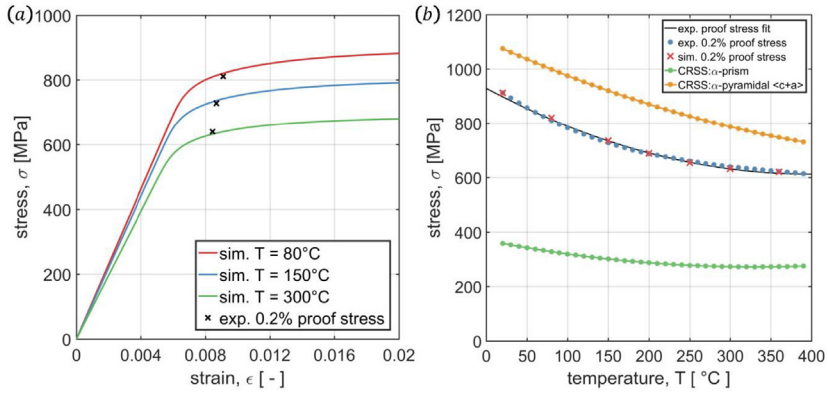

Fig. 3. Temperature sensitivity of IMI834 polycrystal using homogenised α model (a) stress-strain response and (b) 0.2% proof stress. The <*a*>-prismatic and <*c* + *a*>-pyramidal slip system CRSS giving rise to the macro-level averaged behaviour is also shown.

$$\tau_{crss}^{prism} = 0.0009 \times T^2 - 0.5942 \times T + 370 \tag{7}$$

and the <*c* + *a*>-pyramidal slip system CRSS (Williams et al., 2002; Zhang et al., 2015) is given by

$$\tau_{crss}^{<c+a>} = 0.0011 \times T^2 - 1.3801 \times T + 1102.59 \tag{8}$$

which gives the ratio of <*c* + *a*>-pyramidal to <*a*>-prismatic strength as 3:1 at 20 °C. The other slip rule properties are listed in Table 1. Using the calibrated model, the proof stresses at other temperatures, such as 20 °C, 200 °C, 250 °C and 360 °C, show agreement with the experiment as shown in Fig. 3(b), which also shows the resulting temperature dependence of the <*a*>-prismatic and <*c* + *a*>-pyramidal CRSS.

Stress relaxation tests were carried out at 80 °C to validate the rate sensitivity of the model. Two IMI834 tension samples were subjected to strain rates of $7 \times 10^{-3}s^{-1}$ and $1.5 \times 10^{-2}s^{-1}$ to target strains of 0.7% and 1.5% respectively and then held at the target strain for 60s as shown in Fig. 4(a). Fig. 4(b) shows the experimentally observed stress relaxations during the strain holds and the corresponding CP model calculations.

3. Investigation of load shedding in experimental (disc spin) tests using homogenised (α) models

We first consider a representative polycrystal sample with average grain size of 1000μm comprising 343 grains with random texture as shown in Fig. 5. All (α-HCP) grains utilise the slip rule described in Section 2 such that the *average* α-β IMI834 alloy behaviour is reproduced as shown in Figs. 3 and 4. A soft-hard grain pair with respect to the hoop direction is located in the centre of the model as shown in Fig. 5. The model is subjected to the local multi-axial loading conditions corresponding to the experimental (disc spin) tests shown in Fig. 6 at 80 °C with hoop stress along the *y*-direction and axial and radial stresses along the *x*- and *z*-directions respectively (as depicted in Fig. 5(d)). That is, at every location of interest within the disc shown in Fig. 6(a) and (b), the *local* multiaxial stresses during a loading cycle are extracted from a full component-level elastic finite element analysis. These extracted local stress histories are then applied to the representative polycrystal plasticity RVE as boundary conditions, as indicated in Fig. 6. It is therefore assumed that the loading cycle boundary conditions remain unchanged during subsequent cycling. The three rig tests shown in Fig. 6(c) and (d) all lead to failure in the experimental observations resulting from dwell facet nucleation at hard/soft grain orientation combinations at the locations shown in Fig. 6(b).

The CP predicted stress distributions along the path $A - A$' through the soft-hard grain combination as indicated in Fig. 7(a) are examined during the loading histories. The yy-stress is parallel to the primary applied stress (i.e. hoop stress), and is the stress normal to the basal for the hard grain. The resulting distributions before and after the dwell period for the three rig tests are shown in Fig. 7. From the results, a peak stress is developed at the soft-hard grain boundary within the hard grain but there is no observation of stress redistribution, or of load shedding on to the hard grain during the stress hold period. In fact, the results show that there is no slip developed in the adjacent soft grain at all and that therefore the applied loading is not sufficiently high to cause even localised micro-slip in the α-homogenised polycrystal model subjected to disc spin test conditions. A consequence is that the homogenised model is argued to be incapable of capturing the conditions necessary to lead to the dwell fatigue facet nucleation in the three rig tests with truly representative loading. Previous dwell work on titanium alloys using homogenised α-HCP models has typically considered the

Table 1
Slip properties for IMI834 homogenised α model.

$\rho_m(\mu m^{-2})$	$\rho_0(\mu m^{-2})$	ν_D(Hz)	k(JK^{-1})	b(μm)	ΔV(μm^3)	ΔF(eV)
5.00	0.01	1.00×10^{11}	1.38×10^{-23}	2.95×10^{-4}	$23.73b^3$	1.061

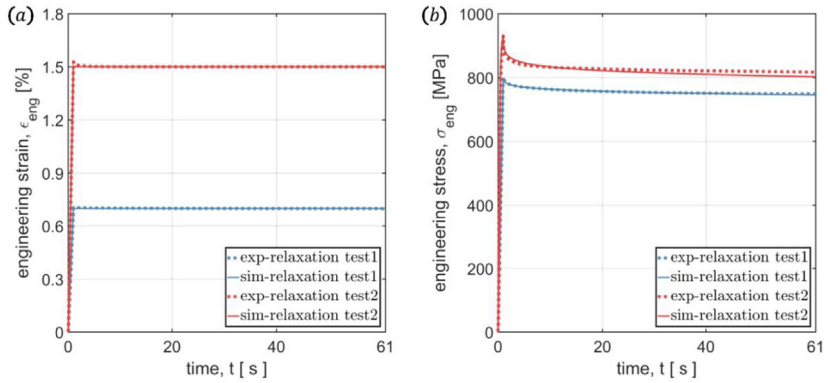

Fig. 4. (a) Loading conditions for two stress relaxation tests: strain increased to target magnitude within 1s followed by 60s holds. (b) Resulting experimental and CP calculated stress relaxations in the two tests.

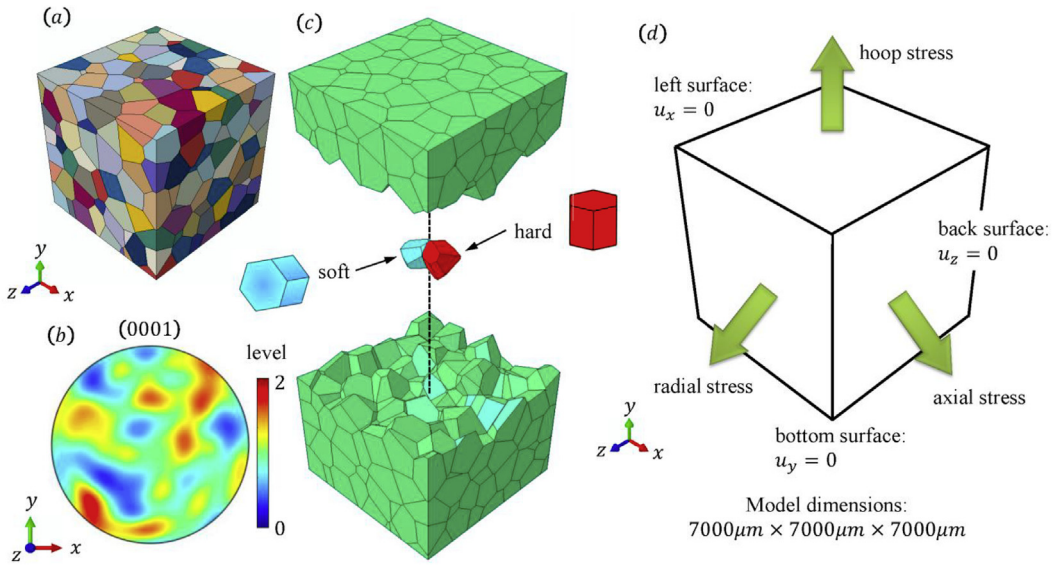

Fig. 5. Polycrystal CP model with a soft-hard grain pair located in the centre. (a) Polycrystal representation; (b) random texture assigned to the model, (c) the location of soft-hard grain pair, and (d) the imposed boundary conditions.

application of higher stresses (as a fraction of yield) such as $1.0\sigma_{0.2}$ on Ti-6Al alloy (Zhang et al., 2015), $0.95\sigma_{0.2}$ on Ti-624x alloys (Zheng et al., 2016b) and $0.95\sigma_{0.2}$ on Ti-6242 alloy (Anahid et al., 2011) and these alloys are, in addition, generally more rate sensitive than IMI834 alloy at 20 °C. For this reason, at the higher applied stress levels, the homogenised models were able to show distinct slip and consequent load shedding. However, the rig tests considered in this study are subjected to lower stresses, e.g. $\ll 0.95\sigma_{0.2}$, which are indicative of in-service loading, for which dwell facets are actually observed. In order to address the observed dwell fatigue failure in the experimental rig tests carried out at lower fractions of yield stress, we argue it is necessary to consider the local plasticity and stress relaxations driven by the local microstructure heterogeneity. Hence, in the following sections, we move to a modelling approach in which the α-β morphology is explicitly represented, and draw comparisons with the α-HCP homogenised approach in this section.

4. Investigation of local stress redistribution and load shedding using α-β microstructure representative CP modelling

The IMI834 alloy from which the rig spin test discs are fabricated has a bi-modal microstructure consisting of a small volume fraction of primary α phase in a lamellar matrix of transformed β phase as shown in Fig. 8(a) and Fig. 8(b). Differing from the homogenised α properties determined in Section 3, the explicit α (HCP) and β (BCC) properties are therefore required in any representative dual phase model. The β phase slip properties are chosen to be consistent with those for Ti-6242 alloy which were carefully determined from micro-pillar compression stress relaxation tests (Zhang et al., 2016), giving β-phase activation energy $\Delta F^{\beta} = 0.334$eV and activation volume $\Delta V^{\beta} = 0.0021b^3$ with Burgers vector $b = 2.86 \times 10^{-4}\mu$m. The α phase slip properties in the dual phase model are then re-calibrated to ensure the macroscopic experimental stress relaxation results shown in Fig. 4 are reproduced

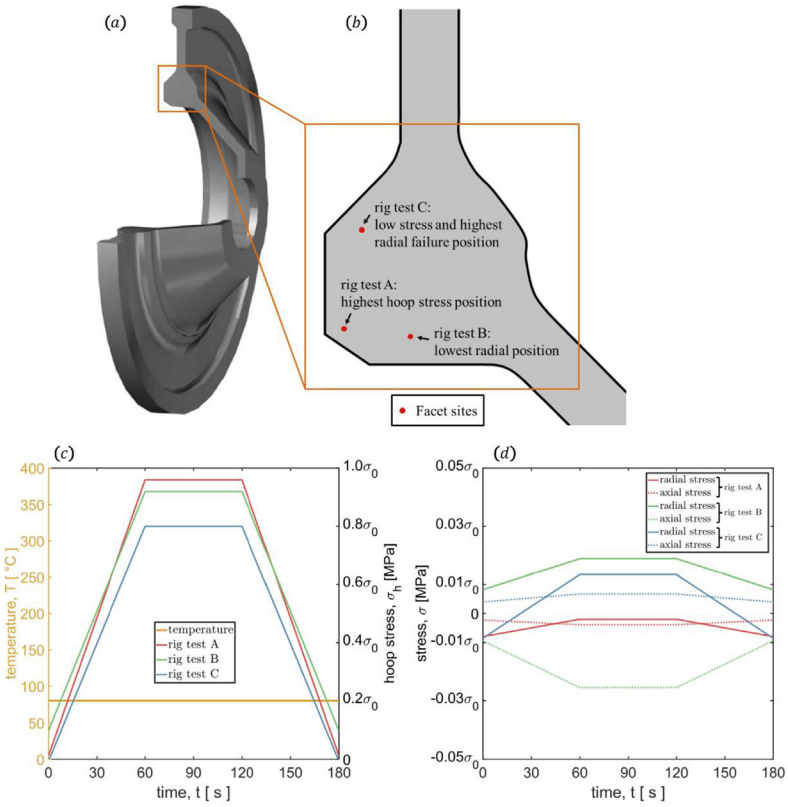

Fig. 6. (a) Schematic illustration of a compressor disc in rig spin tests with 1/4 cutaway (Cuddihy et al., 2017). (b) The observed facet locations for three rig tests. Loading histories of the three tests are shown in (c) temperatures and hoop stresses and (d) radial and axial stresses, which are imposed in the model shown in Fig. 5.

giving α-phase activation energy $\Delta F^{\alpha} = 0.619\text{eV}$ and activation volume $\Delta V^{\alpha} = 20.33b^3$. The α-β CRSS temperature dependence is chosen to be identical to that for the homogenised model, while the macroscopic 0.2% proof stresses as shown in Fig. 3(b) are still satisfied, given by

$$\tau_{crss}^{\alpha-prism} = 0.0009 \times T^2 - 0.5942 \times T + 450.0000$$
$$\tau_{crss}^{\beta} = 0.0009 \times T^2 - 0.5942 \times T + 441.5240 \quad (9)$$

A polycrystal model has been established which approximately replicates a region of the two phase morphology of the IMI834 bimodal and lamellar α-β structure as shown in Fig. 8 with the microstructural model size of 122.5μm × 96.4μm × 4μm. The model incorporates 39 α grains with different crystal orientations and a hard grain crystallographic orientation is assigned to the primary α grain located about in the centre of the region modelled, and a neighbouring secondary α grain is assigned a soft crystallographic orientation favouring a-prismatic slip with respect to the hoop stress loading direction. Crystal orientations of the remaining α grains are chosen to achieve an overall random texture as shown in Fig. 8(d) to reflect the texture associated with the disc test samples. The Burgers Orientation Relationship (BOR) between α and β phase orientations is faithfully satisfied for all neighbouring α-β laths in the model representation. The microstructure is extruded along the thickness direction in the dual phase model as shown in Fig. 8(e). Utilising the explicit dual phase model, the macroscopic temperature and strain rate response of IMI834 alloy continue to be satisfactorily represented as demonstrated in Fig. 9. The average widths of secondary α and β laths are chosen to be 2–3 μm. The model contains 178,422 ten-noded tetrahedral elements (C3D10). It is noted that four-noded tetrahedral elements can sometimes exhibit an overly stiff response resulting from volumetric locking and in the present dual phase model, ten-noded tetrahedral elements are used to avoid the locking problem, but other more rigorous methods to overcome this have been presented by other authors (Cheng et al., 2016).

In this Section, we use this dual phase model to study again the three isothermal rig spin tests and in addition, two thermo-mechanical loadings representative of engine in-service conditions and discuss the mechanisms of thermal alleviation on cold dwell fatigue resulting from the anisothermal temperature loading.

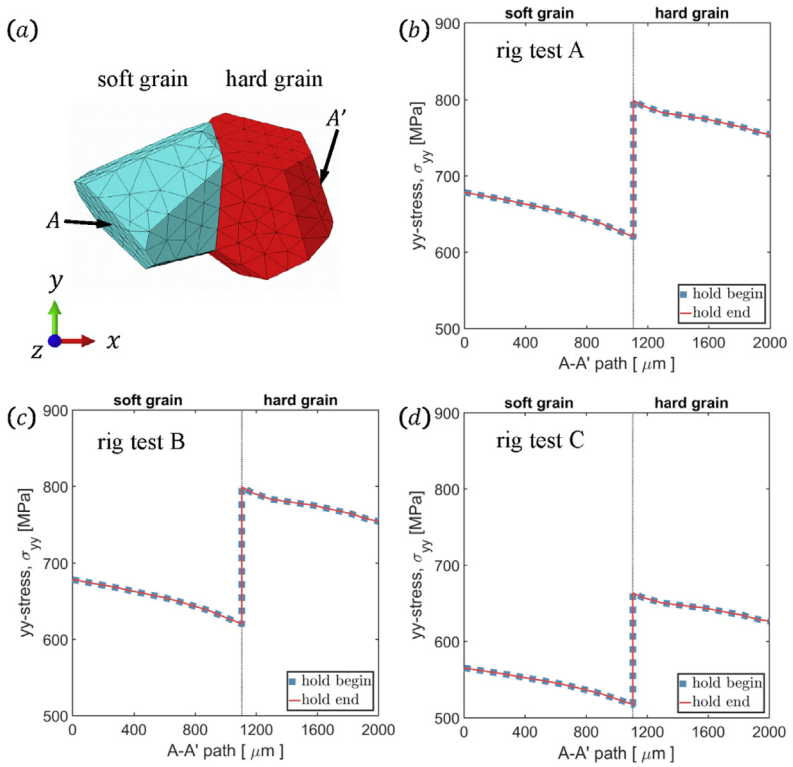

Fig. 7. (a) The location of path $A - A$' through the soft-hard grain combination, and the resulting stress distributions along the path for (b) rig test A, (c) rig test B and (d) rig test C for the homogenised (α) polycrystal model subjected to rig disc spin loading (Fig. 6).

4.1. Assessment of load shedding in spin tests

4.1.1. Load shedding in one loading cycle in spin tests

The three rig spin test loading conditions shown in Fig. 6 are applied to the dual phase model shown in Fig. 8(e) with the hoop stress along the y-direction and axial and radial stresses along the x- and z- directions respectively. The applied stresses are lowest ($<0.8\sigma_0$) for rig test C, so the instantaneous effective plastic strain p developed in the soft grain structure after the initial load-up (but before the stress dwell) is shown in Fig. 10 for this case. The results demonstrate that the explicit inclusion of the complex α-β lamellar microstructure has led to stress states which are sufficiently high to drive the onset of local slip. This is quite contrary to the α-HCP homogenised results presented earlier for which local yield was not achieved, and makes clear the point that in order to capture slip-driven damage processes occurring during dwell fatigue at realistic loading levels (i.e. in-service aero-engine conditions), it is essential to include microstructural detail. The higher loading levels for rig spin tests A and B naturally give rise to greater slip activation. The stress and effective plastic strain distributions along path $B - B$' (Fig. 8(c)) are examined before and after the stress hold periods in order to give indicative load shedding behaviour, and the results are summarised in Fig. 11. Note that path $B - B$' is chosen arbitrarily and does not identify those locations giving rise to the highest stresses resulting from load shedding (see later). The peak stresses developed at the soft-hard grain boundaries for all three tests are higher after the dwell period, thus showing the activation of load shedding in this material at stresses relevant to in-service conditions. Interestingly the load shedding is greatest for rig test B along the considered path (43 MPa) while rig test A gives lower load shedding (38 MPa) in the first loading cycle. This is due to the multi-axial loading conditions such that the radial and axial stresses in rig test B assist the stress redistribution during the hold period. The results also show the role of the β phase laths in perturbing the stress distributions in the soft grains, leading to bands of lower stress (within the β laths) such that higher stresses are generated elsewhere in the soft α laths and hard α grains in order to maintain conditions of equilibrium during the stress hold period.

The locations at the soft-hard boundary (but within the hard α grain) giving rise to the highest yy-stresses have been identified and the corresponding stresses at these locations during the full loading histories (including the stress dwell period) are shown in Fig. 12 for the three rig tests. The basal stresses increase during the stress dwell period due to load shedding by up to 133 MPa for rig tests A, reducing to a stress increase of 44 MPa in rig test B and 19 MPa in rig test C due to the lower applied hoop stress. All three rig tests therefore show stress redistribution (load shedding) from soft to hard grains, reflecting the continuing (cold) creep development in the soft grains. Further cycling therefore leads to more creep accumulation, pushing up further the local stresses on the hard grain, indicating an incubation period for facets to nucleate. The peak stresses (after one cycle) on basal planes developed at the hard grain after load shedding for rig test A is greater than the c-axis direction tensile strength (~1200 MPa). At the end of the unloading stage, the local residual stress remaining in the hard grain is greater than 200 MPa for rig tests A and B, and over 20 MPa in test C,

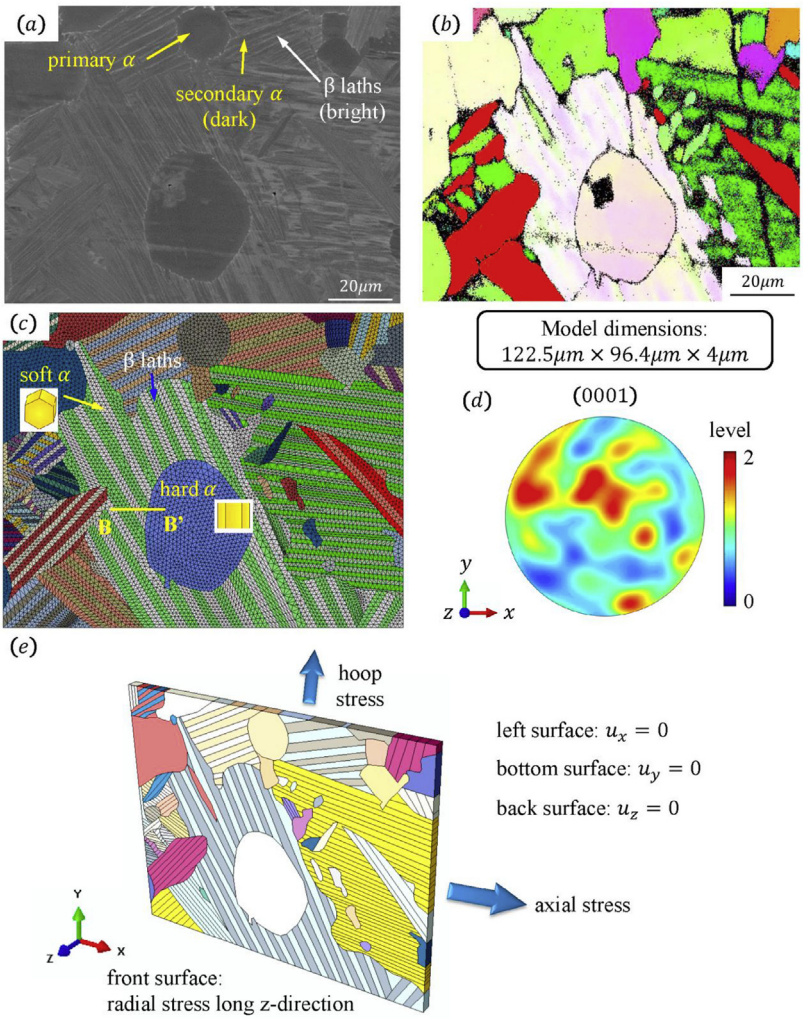

Fig. 8. (a) SEM image of IMI834 alloy shows the bimodal microstructure; (b) the corresponding EBSD map; (c) front surface of the dual phase polycrystal CP model with α-β morphology explicitly represented (d) pole figure showing the overall random texture assigned in the α grains in the model, and (e) the imposed boundary conditions.

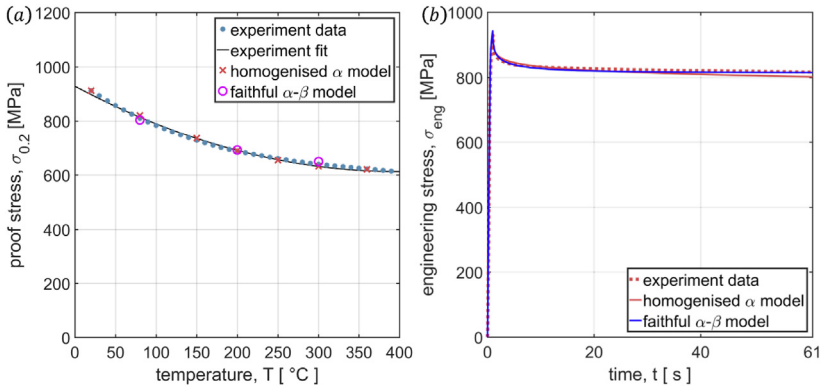

Fig. 9. (a) Temperature sensitivity and (b) stress relaxation of IMI834 polycrystal using homogenised α model and faithful α-β model.

potentially of importance in subsequent cycles driving up stresses normal to the basal as cycling proceeds.

Fig. 13 compares the stress distribution within and surrounding the hard grain before and after the stress hold in the first cycle for rig test A. The stress redistribution from the soft grains causes the yy-stress in the hard grain to increase during the dwell period

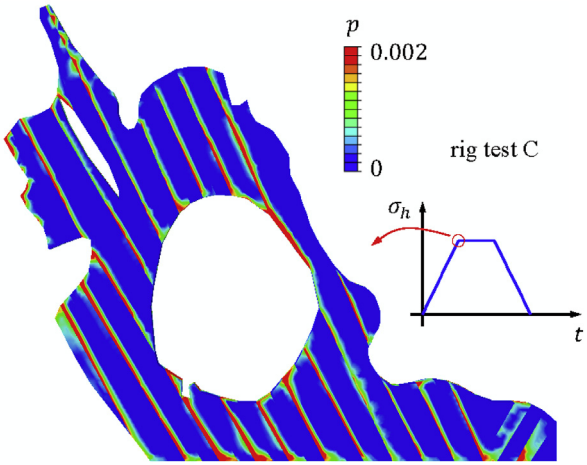

Fig. 10. The instantaneous effective plastic strain p developed in the soft grain structure before the stress dwell in rig test C.

which is argued to be crucial in facet nucleation. Note that in addition, with subsequent cycling and due to the progressively increasing creep accumulation, the stresses continue to rise from cycle to cycle (see later). P1, P2 and P3 in Fig. 13(b) identify the locations of highest *yy*-stress in rig tests A, B and C respectvely. Interestingly, the differing locations for the peak stresses for tests A, B and C result from the change in stress state applied in each test (corresponding to differing locations in the test disc). The high stress concentration spots are generally located at the β lath - soft α - hard α triple junctions due to the local constraint and deformation heterogeneity. The β laths generally display lower stress magnitudes because of the lower β stiffness, but the laths just above and below the primary α hard grain show higher stress than at other β positions (the loading is in the y-direction). Similar behaviour can be observed in the soft α laths, and results from the constraint provided by the hard grain.

4.1.2. Cyclic analysis of experimental (disc) tests

The analysis of the α-β microstructure subject to stress dwell loading has so far been carried out for a single loading cycle, and has established the development of slip accumulation in the soft grain structure adjacent to the primary α grain, stress redistribution on to the hard primary grain, and the establishment of residual stress likely to influence subsequent cyclic behaviour. Hence, a cyclic analysis has been carried out by imposing 100 dwell fatigue cycles using the stress history shown in Fig. 6 for the rig spin tests A, B and C. Attention is now focused on the locations at the hard-soft grain boundary where the yy-stresses were found to be highest (i.e. at locations P1, P2 and P3 in Fig. 13(b)). The peak yy-stresses developed during the hold, and the residual *yy*-stresses in the hard grain are shown as a function of cycles in Fig. 14(a). Both peak and residual stresses are found to increase rapidly in the first five cycles (Fig. 14(c–d)) after which a near-constant rate of increase is then observed. The figures and data indicate the establishment of a progressive increase in the peak stresses within the hard primary α grain with cycles, resulting from the creep accumulation in the adjacent soft grain, in turn resulting from the stress dwell within the loading cycle. Fig. 14(b) shows the average instantaneous effective plastic strain in the neighbouring soft grain for each test case, reflecting this. On the basis of the rate of stress increase observed, the number of cycles required to achieve an increase in peak stress of 100 MPa is 552, 1003 and 500 cycles for rig tests A, B and C respectively. The peak stress for rig test C is observed to grow faster than that for tests A and B, such that although the magnitude of the peak stress for this test is lower than that for rig test B to begin, if the rate of increase remains constant, then the peak stress for test C is expected to exceed that for test B after 2375 cycles. Since the peak stresses at the hard primary grain increase with cycles under dwell fatigue loading at different rates in the three test cases, the disc samples are expected to display differing lives to dwell facet nucleation, despite that they all demonstrate strong load shedding in the first loading cycle. Hence the above results and discussion highlight the progressive nature of cyclic increase of creep in the soft grain, which redistributes stress on to the hard grain, such that this also increases with cycles until such time that the local stress and strain states are appropriate to generate a facet. Anahid et al. (2009) have discussed a possible mechanistic measure for such a process to occur.

In summary, therefore, unlike the α-HCP homogenised CP modelling approach, the full microstructurally representative (dual phase α-β) CP modelling indicates that the local stress conditions associated with the isothermal (80 °C) rig spin tests at the locations identified in Fig. 6(b) give rise to cyclic (soft grain) accumulating creep and (hard grain) increasing basal stresses such that facet nucleation is anticipated at worst-case grain pairings with the appropriate crystallographic orientation combinations. The experimental rig disc spin tests demonstrate that facets nucleate at the locations shown in Fig. 6(b) and that subsequent crack propagation occurs. With this knowledge, we next address dwell fatigue for representative test engine thermo-mechanical loading conditions. We assess whether dwell facet nucleation should be anticipated at worst-case grain orientation pairings under these (realistic) conditions, and examine the potentially important role of the anisothermal engine conditions which possibly give rise to thermal alleviation; that is, a decrease in dwell sensitivity resulting from the temperature fluctuations which occur in the first and subsequent (flight) loading cycles.

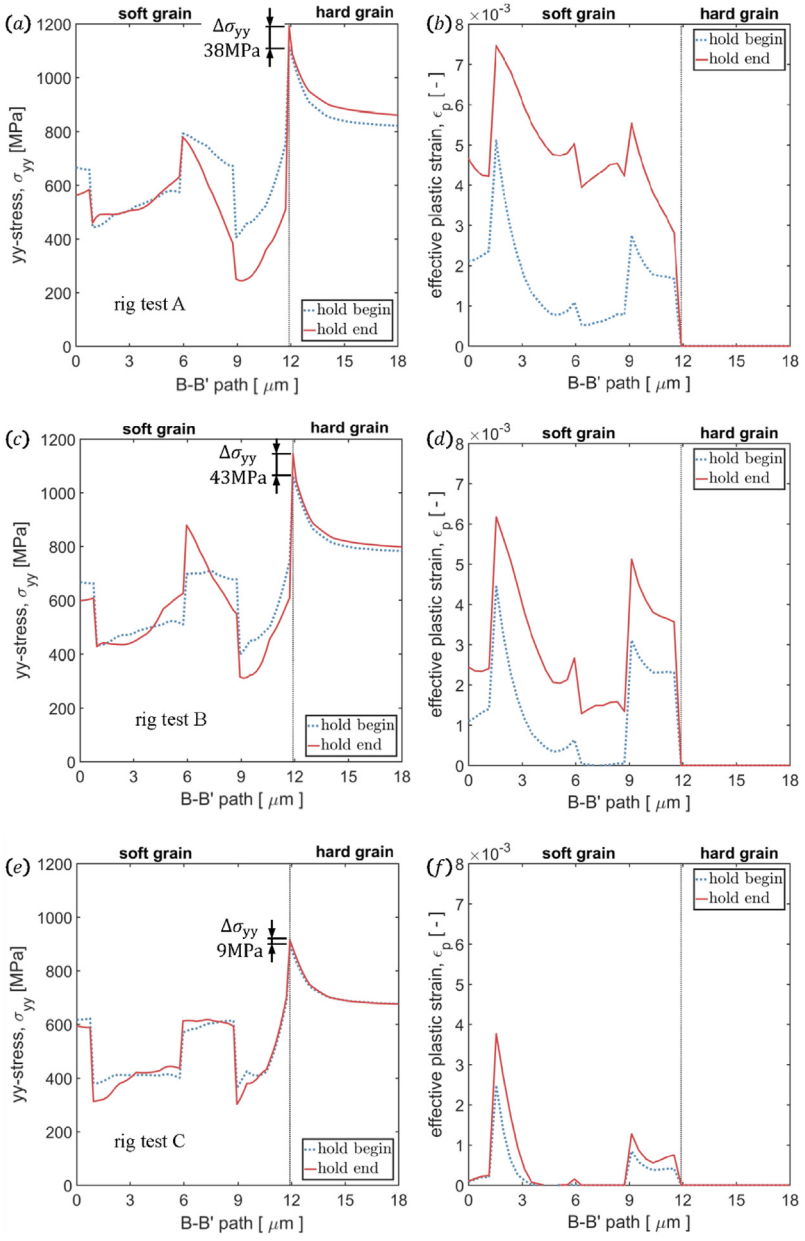

Fig. 11. Stress and effective plastic strain distributions along path $B - B'$ (Fig. 8c) for (a/b) rig test A, (c/d) rig test B and (e/f) rig test C.

4.2. Study of stress development under in-service loading conditions

In order to understand the potential influence of thermal alleviation on cold dwell fatigue, or equivalently to investigate dwell fatigue in compressor discs under realistic in-service loading conditions, the in-service stress and temperature conditions given in Fig. 15 are now applied to the IMI834 α-β dual phase polycrystal model containing worst-case hard-soft grain orientation pairing shown in Fig. 8(c) (as for the isothermal rig disc spin tests). The first conclusion from the modelling of the full cycle (Fig. 15(a)) was that after a time of 2500s, the behaviour had stabilised with no further time-dependent response. The small stress increase occurring at a time of ~13000s naturally leads to changes in stress local to the microstructural features of interest but because the temperature at this stage is high (> 320 °C) and prior stresses had been higher leading to hardening, no further time-dependent change (e.g. load shedding, or creep accumulation) was found to occur. For this reason, we confine reporting of the details of the study to the first 2500s of the loading cycle which is shown in Fig. 15(b) and (c). The highest *yy*-stresses developed in the hard grain as a function of loading history (time) for the two representative loading cycles, termed above Redline and Profile-2 conditions, are shown in Fig. 16. These stresses in the hard grain are very similar for the two loadings (Redline and Profile-2) but the peak stress during take-off is slightly higher for the Redline conditions resulting from the slightly higher applied hoop stress (Fig. 15). During the subsequent

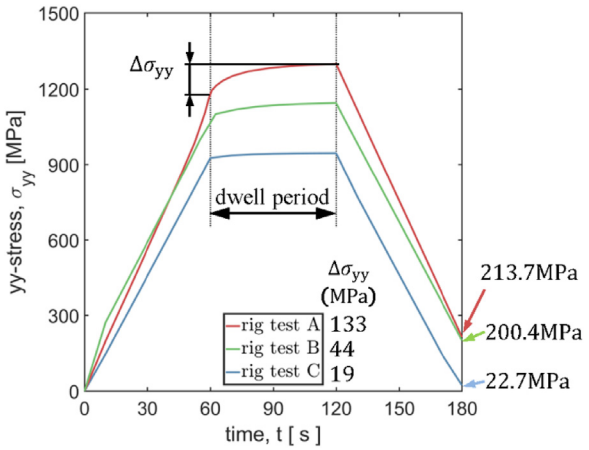

Fig. 12. The *yy*-stress development at hard-soft boundary locations with highest stress in the hard grain during the loading histories.

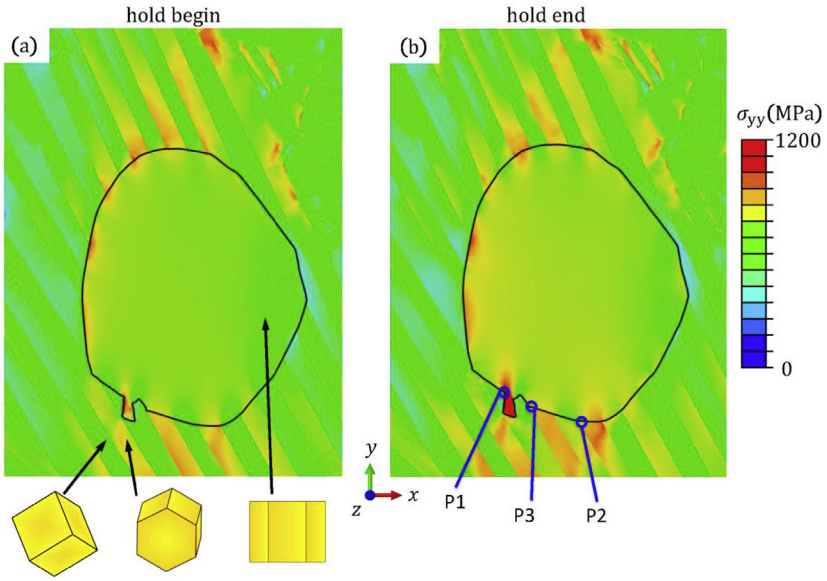

Fig. 13. *yy*-stress distribution around the hard grain (a) before and (b) after stress hold in rig test A. P1, P2 and P3 are the locations of highest *yy*-stress in rig tests A, B and C respectively.

cruise, the temperature and stresses do not change significantly (other than the small excursion at ~13000s which is purely elastic and reflects reduced thrust) for both cases and the maximum stresses in the hard grain do not change significantly. Fig. 16 makes clear that the peak hard grain basal stress remains below ~1200 MPa, compared to the isothermal spin tests which generated stresses of up to 1300 MPa.

Another observation from the in-service loading history is that the stress multi-axiality is different from that in the rig tests: the radial stress exceeds 10% of the corresponding hoop stress for in-service loading while the percentage remains below 2% for the three rig tests. In order to quantify the contribution of the stress multi-axiality to the load shedding, a comparison simulation has been carried out which is similar to Redline conditions but without radial and axial stresses (thereby generating the most extreme uniaxial conditions, worse even than those occurring in the rig tests). The highest yy-stress developed in the hard grain under the modified Redline conditions is shown in Fig. 16. The peak stress during take-off is found to be higher than that under the true Redline conditions. However, as for the latter, any plasticity which occurs is generated during take-off and no further load shedding occurs during the subsequent cruise. Further cyclic analysis also confirms that no additional progressive (cyclic) increasing in hard grain stress occurs, confirming that the modified multi-axiality Redline behaves in a similar manner to the true Redline showing no further load shedding (see later). Hence, the stress multi-axiality contributes only to the development of peak stress during take-off but does not change the reduction in load shedding observed during the subsequent dwell period, which results from thermal history alone.

The stress distributions along path $B - B'$ (Fig. 8(c)) at four selected times indicated during the loading under Redline conditions are plotted in Fig. 17(a). Comparison of responses at times 1 and 2, that is at the start and end of the stress dwell period during take-

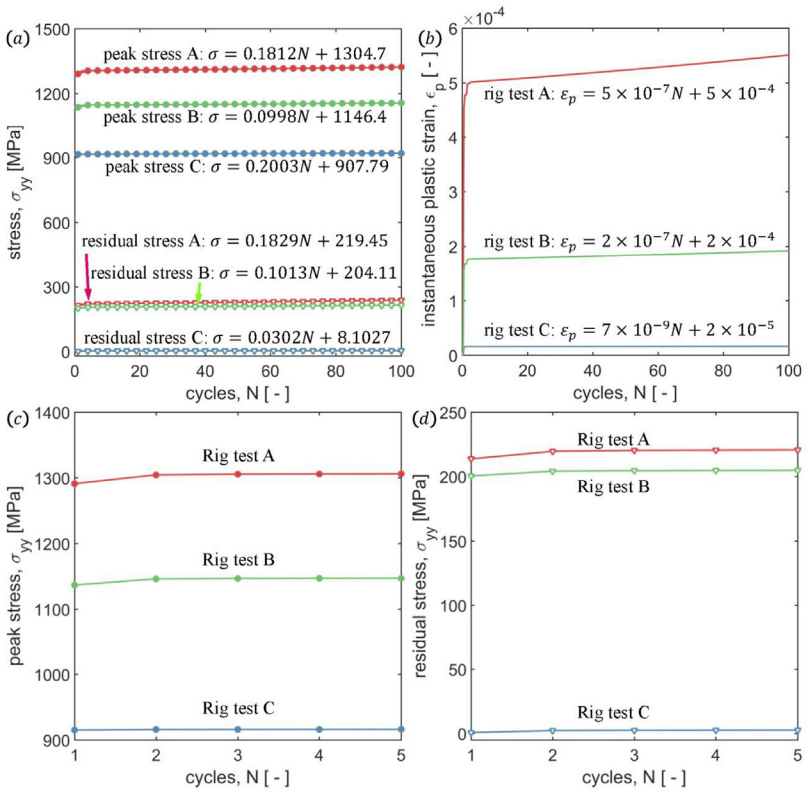

Fig. 14. (a) Peak and residual stress development in the hard grain under 100 dwell fatigue loading cycles (b) the average instantaneous plastic strain in the adjacent soft grain, (c) peak and (d) residual stress development in the first five cycles.

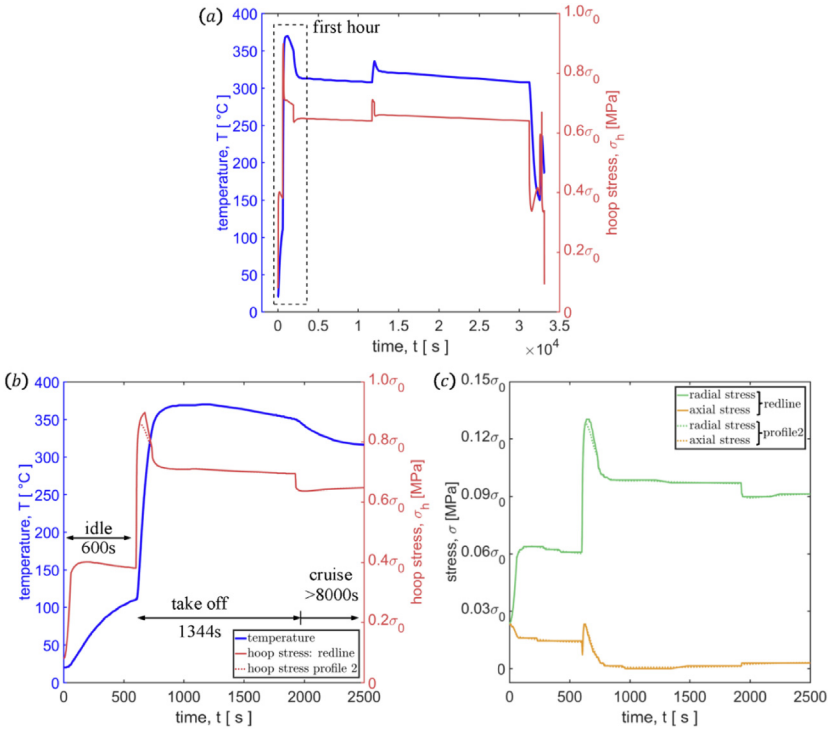

Fig. 15. (a) In-service stress and temperature histories of 9 h long haul flight. Stress and temperature histories for the first 2500s for Redline and Profile-2 in-service engine loading scenarios are shown and (b) gives temperatures and hoop stresses and (c) the radial and axial stresses.

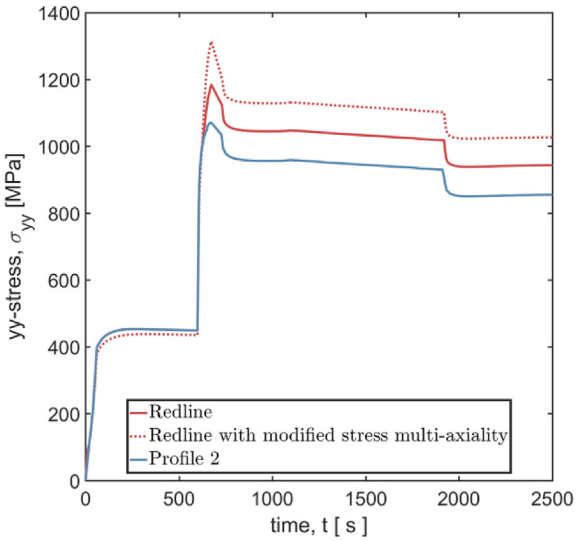

Fig. 16. Maximum *yy*-stress in the hard grain under in-service (Redline and Profile-2) conditions.

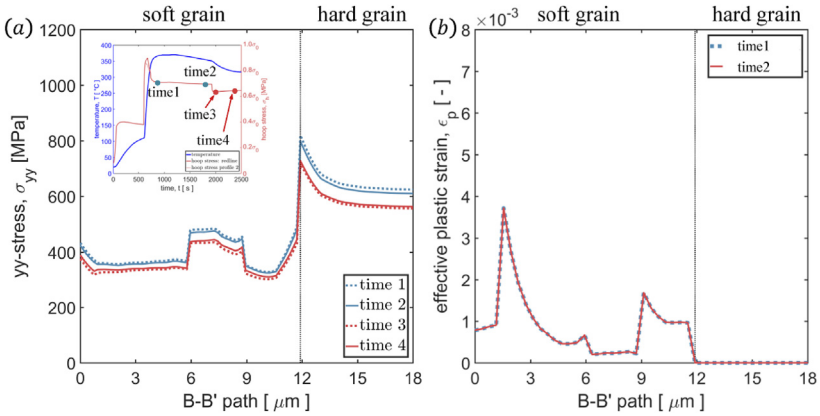

Fig. 17. (a) Stress and (b) effective plastic strain distribution along path $B - B$' through the soft-hard grain combination at the four selected times indicated in the loading cycle (inset) for the Redline loading conditions.

off, show that no stress redistribution (load shedding) from the soft grain structure to the hard primary grain takes place, and that it is significantly different compared to that for the isothermal rig test conditions (e.g. see Fig. 11(d)). The effective plastic strain along path $B - B$' shown in Fig. 17(b) also demonstrates no additional plasticity is generated during the stress dwell period. Comparing to that developed under rig tests shown in Fig. 11 the plasticity under Redline conditions sits between rig tests B and C. Interestingly, the maximum applied hoop stress during take-off in Redline (Fig. 15(b)) is also between rig test B and C (Fig. 6(c)). Due to the higher operating temperature under in-service conditions, even without a dwell period during take-off, local plasticity still develops. However, as a result of the elevated temperature, the equilibrium state is established quickly and no subsequent load shedding occurs during the cruise. The subsequent stress decrease (just before 'time 3') follows simply from the applied load drop. The stress distributions at times 3 and 4 are almost identical demonstrating that the equilibrium state during the cruise has then been established.

In order to quantify the magnitude of the stress redistribution (load shedding) during the Redline loading histories, another comparison simulation has been established which is identical to that for the Redline test case but for which the activation energy (for thermally activated dislocation escape) in the crystal slip rule is set to be very large (i.e. $\Delta F \rightarrow \infty$). Hence, in the comparison test, the strain rate sensitivity is switched off such that no load shedding (or creep) may arise because the plasticity is entirely suppressed. The results comparing the average *yy*-stresses in the hard grain are shown in Fig. 18(a). The magnitude of load shedding can be obtained by taking the difference during the loading history and this is also shown (to a different scale) in Fig. 18(a). The maximum load shedding occurs at the peak stress stage during take-off which is less than 12MPa and much lower than that for the rig tests. Once the cruise stage in the loading history is reached, no further load shedding occurs. We choose a point P in the soft α grain which is close to the soft-hard grain boundary and examine the instantaneous effective plastic strain as shown in Fig. 18(b). The plastic strain is found to initiate at the beginning of take-off and peaks at about 0.004 before the cruise phase begins. Since no further plastic deformation is generated during the cruise, its duration is argued to have no subsequent effect on the fatigue life of the discs (for the

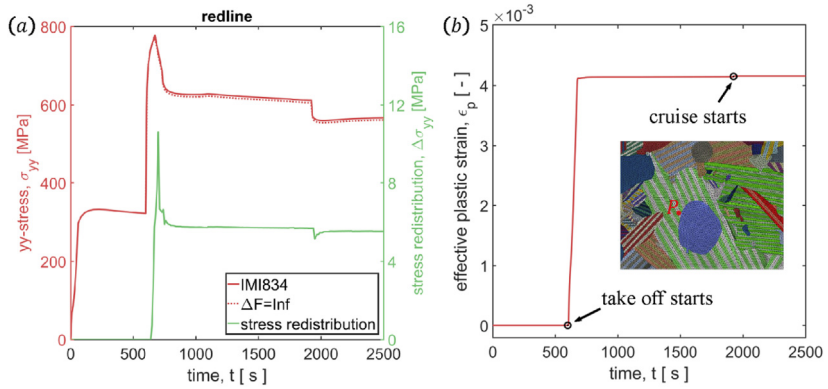

Fig. 18. (a) Assessment of load shedding in Redline using a comparison test with infinite activation energy ΔF. (b) The instantaneous plastic strain extracted from point P as indicated in the sub-figure.

particular loading cycle assessed).

4.2.1. Cyclic analysis of in-service loading conditions

Cyclic loading simulations are also carried out for the in-service loading profiles. Fig. 19(a) shows the cyclic hoop stress and temperature history employed. The first 2500s are chosen to be identical to the Redline test after which, as discussed above, the duration of the subsequent cruise becomes irrelevant so this is reduced substantially and followed by the reduction of applied hoop stress and temperature reflecting landing and the static state to 54 MPa and 20 °C respectively. Note the non-zero static stress is simply the pointwise remaining residual hoop stress. The relaxation period is included to represent engine cool-off after landing. The radial and axial stresses of each loading cycle are also included in Fig. 19(a) and since no further plasticity is expected during landing, these applied component stresses are reduced to zero linearly at the end of the cycle. Fig. 19(b) shows the stress at the location in the hard grain which is spatially the highest, for the 10 loading cycles modelled. A transient stress reduction is seen to occur and the highest hard grain stress is interestingly found to decrease by 360 MPa over the first six cycles in clear contrast to what was observed for the isothermal rig spin tests. The maximum residual stress is found to increase in the first six cycles. In this thermo-mechanical cycle, the local stress concentration region during take-off induces slip and leads to a more homogeneous distribution of the stress with cycling, shown after six cycles in Fig. 20, and the maximum stress is close to 820 MPa which is considerably lower than that for the isothermal rig spin tests, and there is no subsequent increase in peak basal stress with cycles, nor accumulation of creep in the adjacent soft grain. Under in-service thermo-mechanical loading, therefore, the conditions at worst-case hard-soft grain orientation combinations give no indication of leading to progressively increasing hard grain basal stresses nor soft grain creep accumulation and as a consequence, dwell fatigue facets are not anticipated to be nucleated.

5. Discussion

Consideration of the CP-calculated worst case hard grain basal stresses in the three rig tests and the two in-service engine conditions shows that the peak stresses found in the hard grain are higher than the macroscopic yield strength. In (Zhang et al., 2015), the authors demonstrated that creep and load shedding in the α titanium alloy considered diminish when the temperature is

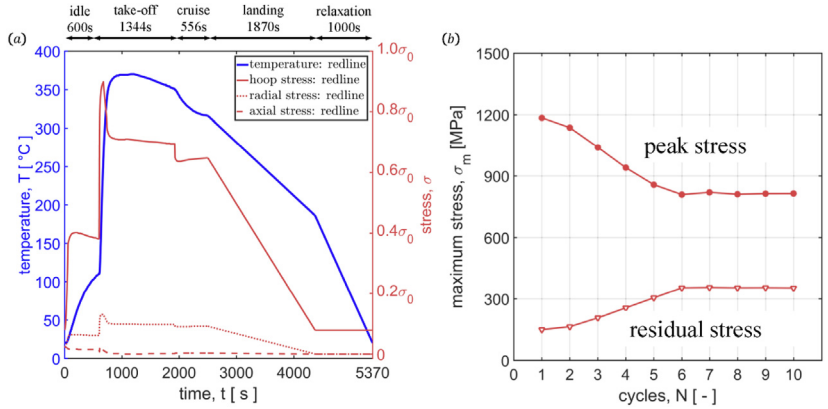

Fig. 19. (a) One loading cycle of the Redline profile applied in the dual phase model, and (b) the development of the peak yy-stress in the hard grain with cycles.

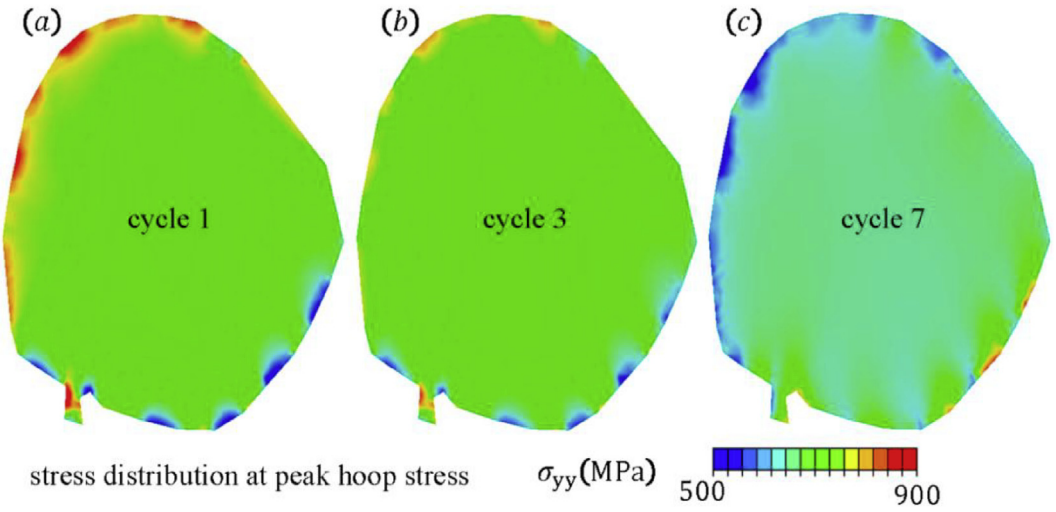

Fig. 20. Stress distribution in the hard grain under peak hoop stress during take-off at (a) cycle 1, (b) cycle 3 and (c) cycle 7.

higher than about 200 °C due to the reduction in the manifestation of the strain rate sensitivity. Fig. 21 shows the peak hard grain basal stresses relevant to the critical disc locations of observed facet nucleation in the three isothermal rig tests and an anisothermal in-service condition respectively in which the line colour represents the corresponding temperature history. The blue colour in Fig. 21(a) for the three rig tests indicates the isothermal conditions in these experiments and the test temperature (80 °C) is known to be one for which the material is very rate sensitive. Hence, dwell sensitivity is expected in the rig tests. To the contrary, the dwell period in Fig. 21(b) occurs at relatively high temperatures, at which load shedding diminishes to negligible levels, since no further cold creep occurs in the adjacent soft grain during the stress hold (since it all takes place within the load-up). Note that this is not to say that the material isn't intrinsically rate sensitive at these (> 300 °C) temperatures; rather, it is the case that the energy barrier to thermally activated dislocation escape is so low that all of the cold creep occurs during the load-up, prior to the stress dwell. This is because there is very limited dislocation pinning by the time the stress dwell is imposed, such that there is no driving force for further thermally activated escape and hence stress relaxation (Zheng et al., 2017b). Hence the alloy is not sensitive to the dwell loading.

Analysis of all facet sites in 22 disc spin tests suggests a critical basal stress associated with facet nucleation might be determined to be about 1200 MPa (Cuddihy et al., 2017), which is also near the c-axis direction tensile strength in single crystal titanium. Other authors have proposed more rigorous (stress-based) criteria for the nucleation of dwell facets (Anahid et al., 2011; Ozturk et al., 2017), but for the purposes of discussion, let us hypothesise that if the local basal stress exceeds the critical (1200 MPa) value, a facet crack may be nucleated. In the three rig tests, the local basal stress in one of them (A) exceeds the critical stress in the first fatigue cycle while in rig tests B and C it does not. However, the rig tests B and C were carried out at strongly strain rate sensitive temperature of 80 °C leading to creep accumulation in the soft grain and progressively increasing basal stress in the primary hard grain and from Fig. 14(a), the peak basal stress in rig tests B and C achieves a level of 1200 MPa after about 538 and 1459 cycles respectively, at which point, according to our simple hypothesis, a dwell fatigue facet would be anticipated to develop. In contrast, the local highest basal stress in the in-service Redline test does not exceed the critical value in the first cycle and since the stress dwell occurs when the temperature exceeds 300 °C, neither soft grain creep nor load shedding on to the primary hard grain is found to occur during dwell, and importantly, the hard grain normal stress has been found not to increase during cycling (see Fig. 19(b)); in fact it reduces and

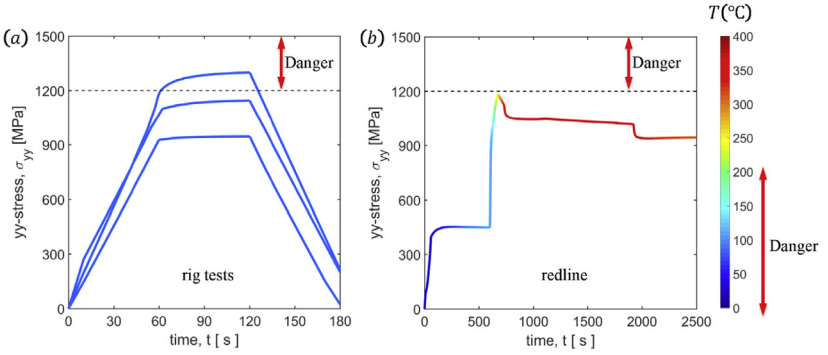

Fig. 21. Predicted peak stresses in (a) rig tests and (b) Redline test. The line colours represent the corresponding temperatures. (For interpretation of the references to colour in this figure legend, the reader is referred to the Web version of this article.)

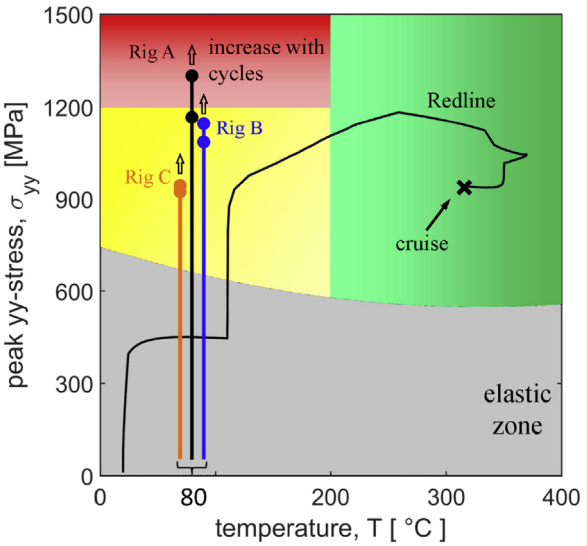

Fig. 22. Peak basal stress against operating temperature map demarcated into dangerous (red), potential threat (yellow) and safe (green) regions with respect to dwell facet nucleation. The CP determined results for the (isothermal) rig spin tests and in-service Redline test *after one loading cycle* are superimposed. (For interpretation of the references to colour in this figure legend, the reader is referred to the Web version of this article.)

saturates by (rate independent) cyclic stress relaxation below the critical stress. For these reasons, dwell fatigue facet nucleation is not anticipated in the in-service (engine) loading conditions.

In order to investigate further the interactions of temperature and stress in cold dwell fatigue, and in particular with respect to the isothermal rig tests and (anisothermal) in-service engine conditions considered in this paper, a peak (hard grain basal) stress against operating temperature map has been generated as shown in Fig. 22, in which three regimes identified as dangerous, threatening and safe have been introduced with respect to dwell facet nucleation. Superimposed on the map are the thermo-mechanical loadings associated with the *first cycle only* of each of four loading scenarios considered: the three rig tests (A, B and C) and the (Redline) in-service conditions. The criteria defining the regions are that a basal (hard grain) stress greater than 1200 MPa is taken to be a necessary condition for facet nucleation (determined from rig spin tests (Cuddihy et al., 2017)), that a temperature in excess of 200 °C inhibits facet nucleation (Zhang et al., 2015; Zheng et al., 2017b), and that soft grain slip is also a prerequisite for facet nucleation (which defines the elastic region shown). However, the diagram is not yet complete in that it shows the loading histories with respect to the demarcations but only for a single first loading cycle. Earlier, it was made clear that there are conditions giving rise to progressive cyclically increasing hard grain basal stress such that a given number of cycles is required in order to drive the basal stress higher than the critical 1200 MPa. Hence the region identified as threatening (yellow) has been included. In addition, for those loading cases for which a progressively increasing hard grain basal stress occurs (rig tests A, B and C), an upward arrow has been included at the loading history termination; where the hard grain basal stress is unchanged (i.e. stable) with further cycles, a cross is shown (in-service Redline).

Hence a peak stress in the loading history entering the red zone indicates a propensity to nucleate a dwell facet. The yellow zone represents the strain rate sensitive temperatures, and if the basal stress developed is located in this region, even if its current magnitude is lower than the critical stress, it should be treated as a threat because the basal stresses are ratcheting up (due to cold creep in the adjacent soft grain during dwell) to exceed the critical stress of 1200 MPa with further loading cycles. The material behaviour relevant to the yellow zone has been studied in some detail (Zheng et al., 2017b) in which thermally activated dislocation escape from obstacles during stress dwell is shown via discrete dislocation analyses to lead to dislocation pile-up at the hard-soft grain boundaries, leading to a gradual cycle by cycle increase in the hard grain basal stress, supporting the CP studies reported here. The green zone in Fig. 22 indicates the safe zone for which the loading is not anticipated to give rise to dwell fatigue. In this zone, the basal stress is not high enough to nucleate a dwell facet in the first cycle, and the stress cannot increase in subsequent cycles due to the diminution of cold creep accumulation and load shedding during dwell at temperature in excess of ~200 °C. The mechanistic basis for this was also studied using discrete dislocation analyses (Zheng et al., 2017b) showing that in these circumstances, dislocation escape from obstacles occurs very rapidly (as a result of a low effective energy barrier to dislocation escape) such that equilibrium is achieved before stress dwell inhibiting load shedding. Titanium alloys subjected to these kinds of loading conditions do not display dwell sensitivity.

In Fig. 22, the three rig spin tests are isothermal and as a result show straight vertical lines. The two circles for each load type (A, B and C) indicate the peak hard grain basal stress before and after stress dwell respectively in the first loading cycle, hence indicating the propensity to accumulate creep in the soft grain and to shed load on to the hard grain. In addition, it indicates that further cycling will lead to increasing hard grain basal stress. Rig test A enters the red zone in the first cycle, and hence dwell facet cracks are nucleated in this test. The maximum stress after dwell in rig tests B and C for the first cycle is located in the yellow zone indicating that the peak stress will increase with cycles, demonstrated by Fig. 14(a). Hence, the peak stresses in both tests are expected to

achieve the critical stress with further loading cycles with the anticipation of dwell facet nucleation. However, the in-service Redline thermo-mechanical loading profile for the first loading cycle shows more complex hard grain stress and temperature variation intersecting both the yellow (threatening) and green (safe) zones. But the behaviour shown occurs just within the first cycle for which the hard grain basal stress does not exceed the critical stress. In addition, it was shown earlier that this loading cycle does not lead to further accumulation of soft grain creep during dwell, nor to increasing hard grain stress with further cycles. Hence it is stable and does not lead to dwell facet nucleation. This is borne out by many empirical observations and tests; dwell facets have not been observed for this loading cycle. Hence the above analysis of the drivers for fatigue facet nucleation are entirely in agreement with the experimental observations that the three isothermal rig spin tests show dwell fatigue, facet nucleation and disc failure, but that the specific in-service thermo-mechanical engine test loading considered does not show dwell fatigue facet nucleation.

The observation that isothermal rig spin tests at in-service levels of stress lead to dwell facet nucleation and a dwell fatigue debit whereas the specific in-service loading which includes the thermal loading (giving combined thermo-mechanical conditions) does not, has led to the introduction of the term thermal alleviation; that is, the inhibition of dwell-sensitive fatigue response as a result of the thermal component of in-service loading conditions. We have demonstrated in this paper that there is a thermal alleviation effect in dwell fatigue and that it contributes to reducing dwell sensitivity by negating the creep accumulation in the soft grain (during dwell) of the worst-case hard-soft grain orientation combination, and the consequent stress redistribution onto the hard grain. In addition, by inhibiting the cold creep accumulation during dwell from cycle to cycle, it eliminates, or substantially reduces the ratcheting process which drives the progressive neighbouring hard grain basal stress increase during cycling such that the conditions to nucleate a basal facet cannot be achieved.

The origin of the thermal alleviation comes from the effect of temperature on key slip properties. Firstly, a-type (prism and basal) slip strengths decrease with increasing temperature, but slip strength for the stronger pyramidal $c + a$ systems decreases more rapidly (Ozturk et al., 2016; Williams et al., 2002; Zhang et al., 2015). As a consequence, the difference between the slip strengths in the hard and soft orientated grain pair reduces with elevated temperature, making the slip behaviour less anisotropic, reducing the stress mismatch across the hard-soft boundary. However, an additional important factor is the change in the manifestation of the strain rate sensitivity with elevated temperature. This has been addressed in the context of crystal plasticity (Zhang et al., 2015) and by Zheng et al. (2017b) using discrete dislocation plasticity. The rate sensitivity at a given temperature is key to both the temperature sensitivity of dwell fatigue itself, but also to explaining the thermal alleviation. The increase in temperature leads to the change in rate sensitivity (for a given strain rate regime) which reduces the soft grain creep accumulation during the stress dwell period and hence the propensity for the progressive cycle to cycle increase of the peak stresses redistributed on to the hard grain basal, thus diminishing the propensity for fatigue facet nucleation.

Finally, we return to the stress levels necessary to drive facet nucleation from the perspectives of modelling (α-HCP homogenised or fully α-β microstructurally representative) and experiment (including in-service disc dwell fatigue). Considering firstly the empirical observations, it is well known that the stresses imposed in lab-based dwell fatigue tests ($>0.9\sigma_{0.2}$) are normally substantially higher than those for which facets nucleate in full-scale disc tests ($\ll 0.9\sigma_{0.2}$). The explanation for why higher stresses are needed to drive facet nucleation in lab-tests is normally that of volume; the volume associated with a disc is very much larger than that for a lab sample such that the probability of the appropriate hard-soft grain orientation combination occurring with the appropriate directionality with respect to the applied loading is much higher for a full-scale engine disc than a small (e.g. 10 mm diameter) lab test sample. This is therefore a size effect and quite different to the parallel but also interesting issue of the need for higher applied stresses to drive predicted slip and facet nucleation in modelling methods. Notably, α-HCP homogenised crystal plasticity methods (as demonstrated above and by other authors) when employed to be representative of complex α-β (e.g. lamellar Widmanstätten or basketweave structures) require higher stresses ($\sim 0.9\sigma_{0.2}$) in order to initiate crystal slip and consequently facet nucleation than are representative of rig tests. But the origin of this is in fact deterministic. That is, α-HCP homogenised CP models fail to account for the highly constrained stress states and deformations generated locally by the geometrical α-β structures, where the slip anisotropies and properties (e.g. slip strengths and rate sensitivities) are different, such that microstructurally faithful and realistic geometric and material models are essential if the local material behaviour (slip, creep accumulation, stress redistribution) are to be captured. As a consequence, for alloy IMI834 considered in this paper, explicit representation of the α-β microstructure has been found to be essential in order for the drivers for dwell facet nucleation to become apparent at the lower stresses empirically observed to be necessary.

6. Conclusions

Empirical observations of dwell fatigue facet nucleation (and its absence) in isothermal rig disc spin tests and for in-service thermo-mechanical test conditions in alloy IMI834 have been analysed utilising thermally coupled, and thermally activated dislocation-based crystal plasticity modelling methods. The following conclusions are presented.

1. In the duplex α-β lamellar microstructured IMI834 alloy, homogenised α-HCP model representations have not been found to provide sufficient local detail to capture the initiation of slip, creep accumulation or stress redistribution which occurs within the α-β microstructure. Representative α-β microstructures with the appropriate phase slip properties, however, do enable the activation of slip, and prediction of observed dwell fatigue facet nucleation at empirically sensible stress levels.
2. In isothermal rig disc spin test models using a representative α-β microstructure with hard-soft orientation combinations, the rate-sensitive material response has been shown to lead to creep accumulation in the soft grain and consequent stress redistribution to the hard grain during stress dwell which increases progressively during cycling. Hence the dwell fatigue facet nucleation

empirically observed at low stress in isothermal spin tests has been explained.
3. In-service engine conditions are strongly anisothermal and have been faithfully represented in the α-β crystal modelling to show that the worst case stresses developed on the hard grain are substantially lower than those for the isothermal spin tests, and crucially that ratcheting does not occur by soft grain cyclic creep accumulation, and nor does the hard grain stress increase with cycles. Hence the empirical observation of the absence of dwell fatigue facet nucleation for these loading conditions has been explained, and the mechanistic basis of what is termed the (dwell fatigue) thermal alleviation has been presented.
4. Temperature plays a key role in cold dwell fatigue, in addition to stress. A dwell sensitivity map has therefore been constructed for alloy IMI834 identifying the regions of (local) stress and temperature over which the propensity for dwell facet nucleation is potentially high, threatening or low.

Acknowledgments

ZZ/FPED acknowledge the financial support by the Engineering and Physical Sciences Research Council for funding through the DARE grant EP/L025213/1 and the HexMat programme grant EP/K034332/1. FPED wishes to acknowledge gratefully the provision of funding for his Royal Academy of Engineering/Rolls-Royce research chair.

References

Anahid, M., Chakraborty, P., Joseph, D., Ghosh, S., 2009. Wavelet decomposed dual-time scale crystal plasticity FE model for analyzing cyclic deformation induced crack nucleation in polycrystals. Model. Simulat. Mater. Sci. Eng. 17, 064009.
Anahid, M., Samal, M.K., Ghosh, S., 2011. Dwell fatigue crack nucleation model based on crystal plasticity finite element simulations of polycrystalline titanium alloys. J. Mech. Phys. Solid. 59, 2157–2176.
Bache, M.R., 2003. A review of dwell sensitive fatigue in titanium alloys: the role of microstructure, texture and operating conditions. Int. J. Fatig. 25, 1079–1087.
Bache, M.R., Cope, M., Davies, H.M., Evans, W.J., Harrison, G., 1997. Dwell sensitive fatigue in a near alpha titanium alloy at ambient temperature. Int. J. Fatig. 19, 83–88.
Cheng, J., Shahba, A., Ghosh, S., 2016. Stabilized tetrahedral elements for crystal plasticity finite element analysis overcoming volumetric locking. Comput. Mech. 57, 733–753.
Cuddihy, M.A., Stapleton, A., Williams, S., Dunne, F.P.E., 2017. On cold dwell facet fatigue in titanium alloy aero-engine components. Int. J. Fatig. 97, 177–189.
Dunne, F.P.E., Rugg, D., 2008a. Lengthscale, orientation and morphology effects in fatigue crack nucleation in polycrystals. In: Advances in Heterogeneous Material Mechanics 2008: Proceedings of the Second International Conference on Heterogeneous Materials Mechanics, June 3-8, 2008, Huangshan, China. DEStech Publications, Inc, pp. 145.
Dunne, F.P.E., Rugg, D., 2008b. On the mechanisms of fatigue facet nucleation in titanium alloys. Fatig. Fract. Eng. Mater. Struct. 31, 949–958.
Dunne, F.P.E., Rugg, D., Walker, A., 2007a. Lengthscale-dependent, elastically anisotropic, physically-based hcp crystal plasticity: application to cold-dwell fatigue in Ti alloys. Int. J. Plast. 23, 1061–1083.
Dunne, F.P.E., Walker, A., Rugg, D., 2007c. A systematic study of hcp crystal orientation and morphology effects in polycrystal deformation and fatigue. Proceedings of the Royal Society of London A: Mathematical, Physical and Engineering Sciences, vol. 463. pp. 1467–1489.
Es-Souni, M., 2001. Creep deformation behavior of three high-temperature near α-Ti alloys: IMI 834, IMI 829, and IMI 685. Metall. Mater. Trans. 32, 285–293.
Evans, W.J., Bache, M.R., 1994. Dwell-sensitive fatigue under biaxial loads in the near-alpha titanium alloy IMI685. Int. J. Fatig. 16, 443–452.
Evans, W.J., Gostelow, C.R., 1979. The effect of hold time on the fatigue properties of a β-processed titanium alloy. Metall. Trans. A 10, 1837–1846.
Ghosh, S., Anahid, M., 2013. Homogenized constitutive and fatigue nucleation models from crystal plasticity FE simulations of Ti alloys, Part 1: macroscopic anisotropic yield function. Int. J. Plast. 47, 182–201.
Ghosh, S., Chakraborty, P., 2013. Microstructure and load sensitive fatigue crack nucleation in Ti-6242 using accelerated crystal plasticity FEM simulations. Int. J. Fatig. 48, 231–246.
Hardt, S., Maier, H.J., Christ, H.J., 1999. High-temperature fatigue damage mechanisms in near-α titanium alloy IMI 834. Int. J. Fatig. 21, 779–789.
Hasija, V., Ghosh, S., Mills, M.J., Joseph, D.S., 2003. Deformation and creep modeling in polycrystalline Ti–6Al alloys. Acta Mater. 51, 4533–4549.
Huang, S., Brown, D.W., Clausen, B., Teng, Z., Gao, Y., Liaw, P.K., 2012. In situ neutron-diffraction studies on the creep behavior of a ferritic superalloy. Metall. Mater. Trans. 43, 1497–1508.
Joseph, S., Bantounas, I., Lindley, T.C., Dye, D., 2018. Slip transfer and deformation structures resulting from the low cycle fatigue of near-alpha titanium alloy Ti-6242Si. Int. J. Plast. 100, 90–103.
Lee, B.-J., Vecchio, K.S., Ahzi, S., Schoenfeld, S., 1997. Modeling the mechanical behavior of tantalum. Metall. Mater. Trans. 28, 113–122.
Ozturk, D., Pilchak, A.L., Ghosh, S., 2017. Experimentally validated dwell and cyclic fatigue crack nucleation model for α–titanium alloys. Scripta Mater. 127, 15–18.
Ozturk, D., Shahba, A., Ghosh, S., 2016. Crystal plasticity FE study of the effect of thermo-mechanical loading on fatigue crack nucleation in titanium alloys. Fatig. Fract. Eng. Mater. Struct. 39, 752–769.
Pawar, R.R., Deshpande, V.T., 1968. The anisotropy of the thermal expansion of [alpha]-titanium. Acta Crystallogr. A 24, 316–317.
Pototzky, P., Maier, H.J., Christ, H.-J., 1998. Thermomechanical fatigue behavior of the high-temperature titanium alloy IMI 834. Metall. Mater. Trans. 29, 2995–3004.
Qiu, J., Ma, Y., Lei, J., Liu, Y., Huang, A., Rugg, D., Yang, R., 2014. A comparative study on dwell fatigue of Ti-6Al-2Sn-4Zr-xMo (x = 2 to 6) alloys on a microstructure-normalized basis. Metall. Mater. Trans. 45, 6075–6087.
Ready, A.J., Haynes, P.D., Grabowski, B., Rugg, D., Sutton, A.P., 2017. The role of molybdenum in suppressing cold dwell fatigue in titanium alloys. In: Proceedings of the Royal Society A: Mathematical, Physical and Engineering Science, pp. 473.
Sinha, V., Mills, M.J., Williams, J.C., Spowart, J.E., 2006. Observations on the faceted initiation site in the dwell-fatigue tested ti-6242 alloy: crystallographic orientation and size effects. Metall. Mater. Trans. 37, 1507–1518.
Song, Z., Hoeppner, D.W., 1989. Size effect on the fatigue behaviour of IMI 829 titanium alloy under dwell conditions. Int. J. Fatig. 11, 85–90.
Venkataramani, G., Kirane, K., Ghosh, S., 2008. Microstructural parameters affecting creep induced load shedding in Ti-6242 by a size dependent crystal plasticity FE model. Int. J. Plast. 24, 428–454.
Williams, J.C., Baggerly, R.G., Paton, N.E., 2002. Deformation behavior of HCP Ti-Al alloy single crystals. Metall. Mater. Trans. 33, 837–850.
Zhang, Z., Cuddihy, M.A., Dunne, F.P.E., 2015. On rate-dependent polycrystal deformation: the temperature sensitivity of cold dwell fatigue. In: Proceedings of the Royal Society of London A: Mathematical, Physical and Engineering Sciences, pp. 471.
Zhang, Z., Jun, T.-S., Britton, T.B., Dunne, F.P.E., 2016. Determination of Ti-6242 α and β slip properties using micro-pillar test and computational crystal plasticity. J. Mech. Phys. Solid. 95, 393–410.
Zheng, Z., Balint, D.S., Dunne, F.P.E., 2016a. Discrete dislocation and crystal plasticity analyses of load shedding in polycrystalline titanium alloys. Int. J. Plast. 87, 15–31.
Zheng, Z., Balint, D.S., Dunne, F.P.E., 2016b. Dwell fatigue in two Ti alloys: an integrated crystal plasticity and discrete dislocation study. J. Mech. Phys. Solid. 96, 411–427.
Zheng, Z., Balint, D.S., Dunne, F.P.E., 2017a. Investigation of slip transfer across HCP grain boundaries with application to cold dwell facet fatigue. Acta Mater. 127, 43–53.
Zheng, Z., Balint, D.S., Dunne, F.P.E., 2017b. Mechanistic basis of temperature-dependent dwell fatigue in titanium alloys. J. Mech. Phys. Solid. 107, 185–203.
Zheng, Z., Waheed, S., Balint, D.S., Dunne, F.P.E., 2018. Slip transfer across phase boundaries in dual phase titanium alloys and the effect on strain rate sensitivity. Int. J. Plast. 104, 23–38.
Zhu, H.X., Zhang, P., Balint, D., Thorpe, S.M., Elliott, J.A., Windle, A.H., Lin, J., 2014. The effects of regularity on the geometrical properties of Voronoi tessellations. Phys. Stat. Mech. Appl. 406, 42–58.